PHYSICAL REVIEW A VOLUME 43, NUMBER 2 15 JANUARY 1991

Stationary convection in a binary mixture

Elisha Moses
Department of Nuclear Physics, Weizmann Institute of Science, Rehovot 76100, Israel
and Department of Physics, University of Chicago, Chicago, Illinois 60637

Victor Steinberg
Department of Nuclear Physics, Weizmann Institute of Science, Rehovot 76100, Israel

(Received 27 April 1990)

We present an experimental study of stationary convection in a binary mixture at positive values of a separation ratio. The interplay between the Rayleigh-Bénard and the Sorét mechanisms of instability and the corresponding boundary conditions gives us the possibility to observe a transition from large- to small-scale structures as well as a transition between patterns with different symmetries. We also investigate an influence of lateral boundaries and the cell geometry on the pattern selection.

I. INTRODUCTION

During the last several years it has been shown both experimentally and theoretically that convection in a binary fluid is a convenient and easily controllable continuous system exhibiting a rich variety of pattern formation and dynamical phenomena in the vicinity of onset.[1] The interplay between heat and mass diffusion is responsible for the richness of dynamical behavior and provides several significant advantages of the system compared to other nonequilibrium pattern forming systems such as Rayleigh-Bénard convection in a pure fluid. First, the convecting binary fluid shows both stationary and oscillatory behavior near onset, depending on the values of the control parameters. The control parameters are the Rayleigh number $R=\alpha g \Delta T d^3/\nu\kappa$ and the separation ratio $\Psi=-(k_T/T)(\alpha/\beta)$ that defines a coupling between temperature and concentration variations [here $\alpha=-(1/\rho)(\partial\rho/\partial T)$ is the thermal expansion coefficient, $\beta=-(1/\rho)(\partial\rho/\partial c)$ is the concentration expansion coefficient, ΔT is the temperature difference, g is the gravity acceleration, d is the cell height, κ is the thermal diffusivity, ν is the kinematic viscosity, and k_T is the Sorét coefficient]. Ψ is controlled externally by varying the mean temperature and concentration of the sample. The physical mechanism responsible for the coupling is the Sorét effect by which an externally imposed temperature gradient in a mixture establishes a concentration gradient in a mass-conserving system. Most of the recent theoretical developments and experimental observations were devoted to oscillatory convection and multicritical behavior near the convective onset, which have not been observed in another system previously. This type of bifurcation occurs at negative values of Ψ. At positive values of Ψ, both the temperature and concentration gradients destabilize the heat conduction state. This leads to a stationary convection. The second experimentally attractive advantage of the convection in a binary mixture is that one can control the relative importance of the temperature or solute gradient in the instability mechanism by varying R and Ψ. Thus in the case of stationary convection in a binary mixture there exist two regimes of stationary convection, each of which is characterized by a different dominant driving mechanism of instability. Close to onset the instability is dominated by the solute gradient (for large enough values of Ψ) and this regime is defined as the Sorét regime. At $\Psi L^{-1} \gg 1$ the critical temperature difference for the convective onset ΔT_c is reduced considerably compared with the critical temperature difference for onset of convection ΔT_p in a pure fluid with the same thermophysical properties as a binary fluid. (Here $L=D/\kappa$ is the Lewis number, the ratio between mass and thermal diffusivities.) Convective flow above ΔT_p is defined as the Rayleigh regime. When the critical temperature differences for both regimes are very different, the two regimes can be isolated unambiguously.

The intriguing feature of the two regimes is the striking differences in nonlinear behavior both in heat transport and in pattern and wave-number selection. The main results of these experiments presented previously (Ref. 2) are the following. Heat transport in the Sorét regime is drastically reduced compared with the Rayleigh regime, as manifested by very different values of the initial slope S of the Nusselt number versus ΔT for the two regimes where the Nusselt number N is the effective heat transport. Depending on the value of Ψ the heat transport is suppressed drastically so that the initial slope S is reduced up to several orders of magnitude compared to that in the Rayleigh regime. This inefficiency in the heat transport occurs for two reasons. First, due to the Sorét mechanism the temperature perturbation amplitude in the convective flow is L/Ψ times smaller than in the Rayleigh regime. Secondly, the boundary conditions for concentration are zero mass flux due to the impermeable boundaries. As realized a long time ago the impermeable boundary conditions for concentration lead to a decrease of the critical wave number of the pattern selected as Ψ increases. This cellular structure with large horizontal extent is similar to that which has been predicted in the case of the Rayleigh-Bénard convection in a pure fluid with low thermally conductive boundaries. In the latter case it was shown theoretically that the convective heat transport across the layer is proportional to the square of the critical wave number, i.e., it reduces considerably when the wave number decreases; similar functional dependence should, probably, exist in the Sorét regime. Thus at large enough values of Ψ both small wave number of the pattern and small amplitude of the temperature perturbations reduce the convective heat transport in the Sorét regime compared with the Rayleigh regime. Another consequence of the impermeable boundary conditions for concentration is that the preferred pattern in the Sorét regime is found to be a square pattern instead of the roll pattern in the Rayleigh regime.[2] Therefore, a binary mixture provides a convective system where the impermeable boundary conditions are equivalent to insulating boundaries in a convective pure fluid.

As a consequence this system gives us a rare opportunity, by tuning the control parameter Ψ, of varying the "thermal" boundary conditions from good conductivity at $\Psi=0$ to perfectly insulating at $\Psi L^{-} \gg 1$, and to study linear and nonlinear properties of the pattern selected. By tuning the second control parameter R at a given value of $\Psi>0$ one can pass from the Sorét to Rayleigh regime and study pattern competition and switching which is achievable only in the stationary convection of a binary mixture.

We reported previously also the observation of a large-scale structure in the Sorét regime close to onset and a transition to a small-scale square pattern at larger R (but still in the Sorét regime).[2] The dynamics of this transition as well as detailed studies of oscillations in a crossover region between Sorét and Rayleigh regimes are discussed in this paper. The paper is organized as follows. A review of theoretical and experimental results on stationary convection in a binary fluid is presented in Sec. II. In Sec. III we describe the experimental procedure. Section IV consists of the experimental results, and we conclude in Sec. V with a discussion. In the Appendix an estimate of the spatial resolution of the shadowgraph visualization is given.

II. REVIEW OF THEORETICAL AND EXPERIMENTAL RESULTS

A. Theory

The predictions of linear theory have been given in the early works[3,4] for realistic boundaries. More recent work has added detailed numerical results for the rigid-rigid boundaries.[5,6] The critical wavelength of convection at $\psi=0$ beings at a value of 3.117, the wavelength of convection in a pure fluid. At $\psi \approx 0$ there is almost no range of R for which the convection is in the Sorét regime. Then the wave number decreases as a function of ψ till it reaches a value of 0 (for infinite layer). The decrease to zero occurs at a value of ψ where the convection is in the pure Sorét regime.

The phenomenon of $k \rightarrow 0$ gives an indication as to the kind of physics that is going on. In the Sorét regime the system is an exact analog of convection of a pure fluid in a cell that has *perfectly insulating boundary conditions* at top and bottom. This is because the boundary condition on the concentration field at the vertical boundaries is one of no-flux, impermeable boundaries. This corresponds to the case of no heat flux, or insulating, conditions for the temperature field. The result of $k=0$ is one that has been obtained for the case of the Rayleigh regime with insulating boundary conditions.[7] Intuition for the large structure is more apparent in the insulating boundary case. Since heat cannot be transferred from the bottom plate to the top plate through the boundaries, the heat flux must be convected to infinity.

Since the temperature and concentration gradients cooperate to destabilize the system, the critical Rayleigh number is reduced. It begins at 1708 for $\psi=0$ and decreases as a function of ψ. Reference 6 gives a formula for this decrease that depends on the critical wave number. For $k=0$, Ref. 4 showed that the behavior goes as $R=720L/\psi$. For the Lewis numbers relevant to our experiment $k=0$ occurs at $\psi \approx 0.03$. Figure 1 shows the phase diagram with the critical R curve relevant to our values of the Lewis number, along with a summary of our experimental results. Circles denote the first point at which we visually resolve the convective structure in the 1:4:12 cell, and squares denote the point at which rolls appear in the same cell. For $\psi=0.21$ we present the division into the various regimes described below. The data incorporate information from several different cells, and the separating lines are intended mainly as a guide to the eye.

The main prediction of theoretical works in the past regarding the Sorét regime lies in an evaluation of the Nusselt number (N) behavior. The convection is extremely ineffective in transporting heat. The initial slope of N versus $\epsilon=(R-R_c)/R_c$ is given for the unrealistic case of free-free boundaries as[8]

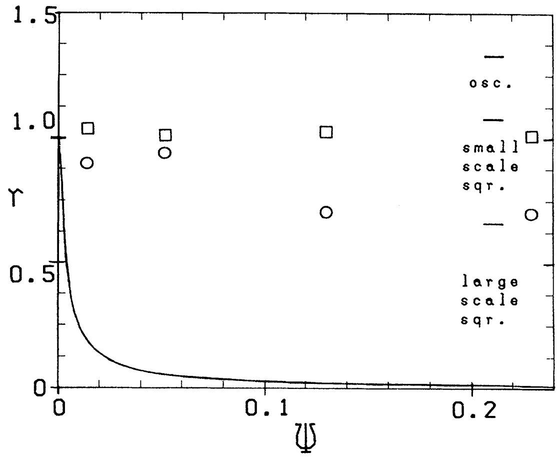

FIG. 1. (ψ,R) phase plane with the critical R curve for $L=0.66\times10^{-3}$. Circles (squares) denote the first point of squares (rolls) in the 1:4:12 cell. The division into different regimes is for measurements at $\psi=0.21$.

$$S \equiv \frac{N-1}{\epsilon} = 2[1+\psi(1+L^{-2})][1+\psi(1+L^{-2}+L^{-3})]^{-1} .$$

For Lewis numbers relevant to our experiment this value is predicted to be on the order of 10^{-2}, versus about 1.4 for the Rayleigh mode in an infinite system of pure water (this changes to $S \approx 0.7$ for water in the finite cells we use).

Numerical simulations of a five mode truncation[9] similar to the three mode truncated Lorenz model have shown that a marked change in the effective heat transport occurs once the Rayleigh regime is reached.[10] At ΔT_p, the temperature difference where convection due to thermal modes would occur for a pure fluid with similar thermophysical properties, S changes over to a value similar to that of the Rayleigh mode for that fluid.

Since until recently no treatment of the pattern selected in the Sorét regime existed in the literature, we used the analogy with thermally insulating boundaries to obtain information on the preferred states. It was shown[11–13] that for perfectly insulating boundaries the long wavelength can be used to evaluate the stability of the various patterns. The usual roll pattern becomes unstable to perturbations at a right angle to the roll, to a set of perpendicular rolls. This square structure was shown[14] to persist for boundaries that are not perfectly insulating. The insulation is measured by the Biot number B, the ratio of the boundary's thermal conductivity to that of the fluid's. This work predicted a transition from the state of square patterns to that of the usual roll one as a function of B and P. For the Prandtl numbers relevant to our experiment this transition occurs just above the value of $B=1$ (for low P the rolls are preferred down to very low values of B). Even more important, a transition was shown to occur as a function of B, from $R_c=1708$ and $k_c=3.117$ at $B=100$ to $R_c=720$ and $k_c=0.6$ at $B=0.001$ (and of course $k_c \rightarrow 0$ as $B \rightarrow 0$). If we were to ramp B up in a continuous way from 0 to ∞, at $B=1$ we can expect a square pattern, but with large ($k \approx 2.6$) wave number. We should add here the obvious caveat that k cannot go below l^{-1}, where l is the cell length, and by $k \rightarrow 0$ we naturally mean the lowest k available in the finite system.

Returning to convection in binary mixtures, the above discussion gives the picture we should expect as we go from the Sorét to the Rayleigh regimes. We associate the Sorét regime with the $B=0$ limit (no-flux, impermeability insulation), and the Rayleigh regime with the $B \rightarrow \infty$ limit (experimentally $B \approx 100$ for the top plate and $B \approx 1000$ for the bottom plate). We should see a square structure of large extent for the Sorét regime, and a transition to smaller wavelength and a roll structure as we cross over to the Rayleigh regime. A binary mixture gives us a unique opportunity in two respects. First, we can realize the analog of perfectly insulating boundaries that can never be achieved for convection with thermal boundaries. Second, we can make a transition from the limit of zero B to the limit of infinite B in two distinct ways: first, by raising R continuously for one given (large enough) ψ, and second, by staying close to threshold (small constant R) and changing ψ from very large and positive to zero.

The recent interest in binary mixtures has spurred theoretical approaches to the problem of planform and heat transport in the positive Ψ case. Silber and Knobloch[15] used a classification of the allowed planforms to show that the impermeability is necessary for the square pattern to appear. This actually confirms our original idea.[2]

Müller and Lücke[16] used a ten mode truncation in a Lorenz-like model to incorporate the possibility of a second, perpendicular set of rolls. They give a comparison of the amplitude of the thermal and concentration modes, and show that the field that is linked to concentration is dominant in the Sorét regime. In the Rayleigh regime the temperature mode becomes stronger by orders of magnitude. They were also able to reproduce the oscillations between rolls and squares. This work also gave results on N, the form of the oscillations, and their frequency, which correspond reasonably well to the results we present below.

A controversial point that Müller and Lücke make is that the squares are unstable to rolls, and that a forcing from the horizontal boundaries (a fieldlike term in the equation) is necessary to stabilize the square pattern. This result is questioned by Knobloch,[17] who uses bifurcation theory to show that, at least on a square lattice, the square rolls are indeed stable. Knobloch also notes that the top and bottom boundary conditions need to be symmetric, but this is indeed our case, since non-Boussinesq effects in the Sorét regime should be very small.

B. Experiment

Traditional experiments that have probed the region of stationary convection in binary mixtures have all come up with similar results. These experiments can be characterized as basically heat-flow measurements, and they focus on monitoring the transition to convection through its effect on N. Early attempts are reported in Ref. 3 where no sign of the transition to the Sorét regime is found. More recent experiments[10,18–20] on ^{3}He-^{4}He mixtures confirmed this result, with much better resolution on S. These experiments found the transition to large S at the critical temperature ΔT_p of the Rayleigh mode of a pure fluid with similar thermophysical properties. They found a small slope leading to the transition at ΔT_p, but this slope was only a precursor to the Rayleigh regime. It did not appear along the full Sorét regime, nor was it observed at onset of the Sorét mode as theory predicts. Reference 20 reports a variety of transitions along the Rayleigh regime, such as we will see can be attributed to their use of a cylindrical cell. This geometry is particularly susceptible to pattern changes due to the mismatch between the induced square pattern and the cylindrical symmetry of the boundaries.

Experiments have also been conducted to test the patterns selected by insulating boundaries for the Rayleigh mode in the pure fluids. In an experiment on mercury[21] with boundaries of resin $B=4.7$, a medium initial S leading to a changeover to the usual S was observed. Spatial information was obtained by a grid of 25 bolometers, from which evidence of a three-dimensional structure was reconstructed. Although not a square structure, this is a pattern of large extent (filling Ref. 21's cell of aspect ratio 4). Downflow occurs at midcell, while flow at the boundaries is modulated on the scale of the cell length.

The introduction of visualization using the shadowgraph technique in an experiment[22] on silicon oil for $B=7$ and 250 gave surprising results when a square pattern was observed for these values of B. This pattern had a characteristic size of the usual Rayleigh regime ($k \approx \pi$). A transition to the usual roll pattern occurred via periodic alternation in amplitude of the two perpendicular sets of rolls that comprise the small square structure. The oscillations became more and more asymmetric, till only one of the two sets of rolls remained, and the convection pattern was dominated by one set of rolls. Since the silicon oil used is a multicomponent liquid, we now understand these phenomena as stemming from the effect of the binary mixture rather than from that of the insulating boundaries.[23]

A confirmation for the existence of the large-scale structure can be found in a laser Doppler velocimetry (LDV) study of convection in a water-isopropanol mixture.[24] When heated from above the convection is always solely driven by concentration gradients and is in the pure Sorét regime. In this region of phase space the results of Platten, Villers, and Lhost point to a large-scale structure, on the order of the cell size (although it is discussed in that work in terms of two large rolls). In the region of $\psi > 0$ and heating from below they found a small slope S for the order parameter (velocity in the x direction). The slope is about three orders of magnitude less than that in the Rayleigh regime.

Following up on this, Lhost and Platten have measured the horizontal component of the velocity in the Sorét regime, showing it to be significantly different from zero, while the vertical component was within their noise. This velocity was extremely small, and compatible with the amplitude, expected from the large-scale flow in the Sorét regime. This seems to indicate that they are viewing the large structure $k \simeq l^{-1}$ that we have observed near onset.

A further work that probes the structure of the flow at positive Ψ is that of Bigazzi, Ciliberto, and Croquette[25] in a mixture of tetrachlorocarbon and methanol. In this work the large-scale structure is not observed. The square cellular structure is picked up when the wave vector is at the peak corresponding to $k=k_p/2$ (as described below). They study in detail the evolution beyond this stage, and give a full description of the oscillations in the Rayleigh regime. They identify the mechanism leading to the oscillations as a propagating wave, a mode predicted theoretically by Linz *et al.*[26]

III. EXPERIMENTAL PROCEDURE

The experiments were done on ethanol-water mixtures with weight concentrations 29.6%, 31%, 35%, and 40% of ethanol at a top plate temperature of 25 °C. The apparatus has been described previously.[1] Since the instability is dominated by spatial features we used several cells of different geometries. Most of the heat-transport measurements reported and part of the pattern observations were done in a quasi-1D (one-dimensional) rectangular cell 2.98 mm high, 12.0 mm wide, and 36.0 mm long (the aspect ratio is 1:4:12). This cell of rectangular dimensions gives preference to the set of rolls perpendicular to the long direction. Thus we could see behavior in which competition was suppressed. To give equal strength to both sets of rolls we used a large square cell with $d=1.8$ mm and aspect ratio $\Gamma=24$ ($\Gamma=l/d$). A small square cell with $d=2.2$ mm and $\Gamma=8.9$ was used to determine the stability against long-wavelength perturbations. The effect of a mismatch between the symmetry of the pattern and the symmetry of the cell was observed in a circular geometry cell with $d=1.8$ mm and aspect ratio 20. The use of relatively thin cells gave excellent resolution in shadowgraph measurements. In the large square and in the circular cell we were even able to see by eye the convection patterns for values of ΔT at which roll patterns were observed. However, the small height also had the effect of decreasing the resolution in heat transport. This is because the bath water that stabilizes the cell temperature has to flush away the heat flux that passes through the cell, and this is proportional to $(\Gamma/d)^2$.

We use recently measured[27] data on ψ and D along with data found in the literature (see references cited in Ref. 27 to estimate L and P). We find that L varies from 7×10^{-3} at 29.6% to 4.5×10^{-3} at 40%. P varies from 23 at 29.6% to 27 at 40%. Values of ψ extrapolated from Ref. 27 are $\psi=0.015$ (29.6%, 25 °C), $\psi=0.050$ (31%, 25 °C), $\psi=0.128$ (35%, 25 °C), $\psi=0.230$ (40%, 25 °C), and $\psi=0.210$ (40%, 30 °C). These values for ψ are 50–100 % larger than our previous estimates, which were based on existing data in the literature. The values of L are smaller by a factor of about 3 than our estimates based on the same literature. The L dependence is important, since the critical R and k show singularities at small L.

IV. RESULTS

We divide this section into five parts. First, we demonstrate the division into the Sorét and Rayleigh modes by looking at the Nusselt number behavior. We then proceed to deal with the existence of a large-scale structure close to onset of convection, deep in the Sorét regime. We follow this by describing the appearance of the small-scale structure, which enhances in strength as the Rayleigh mode becomes dominant. The fourth part deals with the oscillations that occur at the transition from the Sorét regime to the Rayleigh one. These oscillations are inherent to cells with symmetry under rotations of 90°. Finally, we discuss the implications of a restrictive geometry. The region of pure roll structure deep in the Rayleigh regime is dealt with only in passing.

A. Heat-transport measurements

In Fig. 2 we show the results of heat-transport measurements in the rectangular cell for all samples and for the large square cell with aspect ratio $\Gamma=24$. For all

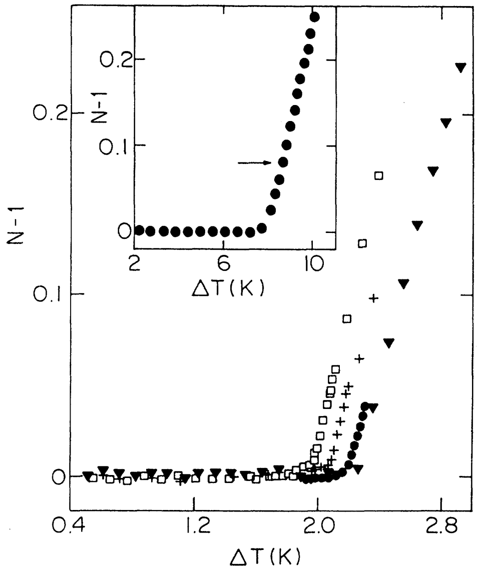

FIG. 2. Convective contribution $N-1$ to heat transport as a function of the temperature difference ΔT across the rectangular cell: (a) squares, 40 wt. %; (b) crosses, 35 wt. %; (c) solid circles, 31 wt. %; (d) triangles, 29.6 wt. % of ethanol. In the upper left corner sample of 40 wt. % in the large square cell. Arrow points at set-in of oscillations.

curves we observe an essentially zero initial slope of N versus ΔT. We relate this region of negligible slope in $N-1$ versus ϵ with the domination of convection due to concentration, i.e., the Sorét regime. The slope changes dramatically at values of ΔT_p that correspond to the critical temperature difference ΔT_p for a pure fluid with the same thermophysical properties. The slope we measure is $S \approx 0.74$–0.77. The exact value of the S depends on Γ, and these are the values we observed for these aspect ratios when using water as the convecting fluid. The expected transition temperatures ΔT_c for the Sorét regime for $d=0.298$ cm and $T=25\,^{\circ}\mathrm{C}$ are approximately 0.5 K (29.6%), 0.2 K (31%), and ≤ 0.05 K (35% and 40%). For $d=0.18$ cm, $C=40\%$ and $T=30\,^{\circ}\mathrm{C}$, ΔT_c is about 0.15 K.

The best test of the slope can be obtained in the large square cell, where we see no deviation from zero slope along up to about 7 K. A slope as small as 10^{-3} over 6 K with a crude estimate of $\Delta T_c = 1$ K would give a change of 0.006 in $N-1$, well within our measurement capabilities. However, due to uncertainties in the calibration of the thermal conductivity of the high density polyethylene (HDP) cell over the range of 7 K, we give an upper limit on $S \leq 0.02$. These uncertainties stem from the nonlinear dependence of the thermal conduction of HDP on temperature, on the small range of temperature along which we can be sure that we are in the conduction state and measure the thermal conductivity of the mixture, and from an uncertainty in the data from the literature on the temperature dependence of the thermal conductivity of our mixtures and cell material.

We can use the results of Fig. 2 to extract ΔT_p. We find for the rectangular cell $\Delta T_p = 1.95$ K ($C=40\%$, $T=25\,^{\circ}\mathrm{C}$), $\Delta T_p = 2.06$ K ($C=35\%$, $T=25\,^{\circ}\mathrm{C}$), $\Delta T_p = 2.18$ K ($C=31\%$, $T=25\,^{\circ}\mathrm{C}$), $\Delta T_p = 2.25$ K ($C=29.6\%$, $T=25\,^{\circ}\mathrm{C}$), for the $\Gamma=24$ square cell $\Delta T_p = 8.02$ K ($C=40\%$, $\bar{T}=30\,^{\circ}\mathrm{C}$), for the $\Gamma=8.9$ square cell $\Delta T_p = 4.82$ K ($C=40\%$, $\bar{T}=27\,^{\circ}\mathrm{C}$), and for the $\Gamma=20$ circular cell $\Delta T_p = 8.2$ K ($C=40\%$, $\bar{T}=30\,^{\circ}\mathrm{C}$), with $\bar{T}$ the mean ambient temperature. Deviations between the circular and square $d=1.8$ mm cell can be attributed to the imprecision in estimating the transition point due to the rounding near the transition, and to slight differences in the pressure used to seal the cell, leading to differences on the order of 1% between the height of the two cells. The results above give agreement to about 2% with the theoretical value for the critical Rayleigh number in pure fluids $R_c = 1708$. In what follows for clearer representation and easier comparison we use this result to measure all ΔT in units of $r = R/1708$.

Although we can give only an upper limit on S for the Sorét regime, we have been able to observe in the shadowgraph images patterns very close to the convective threshold (see below). This strengthens the idea that we are observing convection in which concentration is dominant, and the amplitudes to be monitored are not those of temperature. This suggests that the right estimate for S should be from a direct measurement of the amplitudes, via laser Doppler velocimetry or a related local measurement technique of the velocity and concentration, as done in Ref. 24. Using the results of Ref. 24 in a crude translation from order parameter to N would indicate that the actual slope is of order 10^{-4}, which would lie far below our upper limit, and could explain why we do not observe it.

B. Large-scale structure

In dealing with the signals of the Sorét regime we must remember the limitations of our measuring system. The flow is dominated by motion of the concentration, and the temperature field contributes very little to the convective motion. Therefore the shadowgraph technique is our only tool, and this signal is dominated by changes of density due to concentration alone. The shadowgraph signal is proportional to the second derivative of the field of the refraction index, and for a sinusoidal signal this implies that the signal of small wave number k is suppressed (by a factor of k^2). For an estimate of the possible resolution in our measurement, see the Appendix.

Secondly, we must take into account the characteristic time needed for the concentration gradient to relax. This time is extremely long for the large cells we use. For example, at an aspect ratio of 24 and $L = 4.5 \times 10^{-3}$ the horizontal diffusion time scale $\tau_{h,D} = \Gamma^2 d^2 / D$ is about 48 days. This should be compared with about 5 h for the horizontal thermal relaxation time $\tau_{h,T} = \Gamma^2 d^2 / \kappa$. Obviously we did not wait anything near these times between successive steps in the temperature difference. However, when we talk about vertical diffusion times at $d=1.8$ mm (as is the case for the $\Gamma=24$ cell) then $\tau_{v,D}$ is 2 h. This is, in our opinion, the reason the large-scale structure did

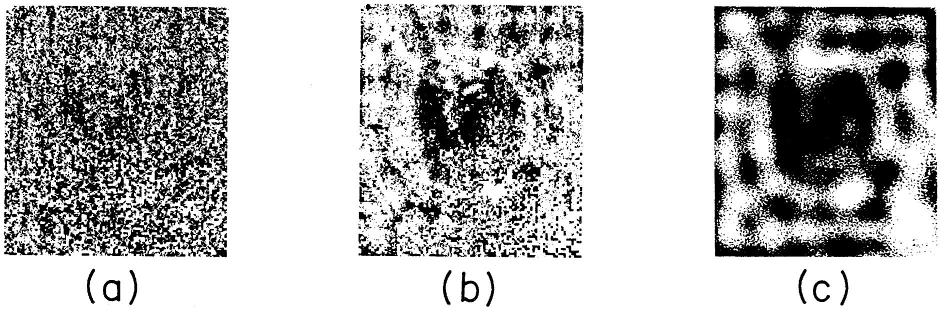

FIG. 3. Flow patterns in the $\Gamma=24$ square cell at low r. (a) 40 wt. % of ethanol, $r=0.012$ ($\Delta T=0.11$ K). (b) 40 wt. % of ethanol, $r=0.16$ ($\Delta T=1.43$ K). (c) Image of (b) after filtering by a truncation in Fourier space.

not in all cases dominate the symmetry of the small-scale structure that followed.

We present first evidence for the large-scale structure in the large square cell ($\Gamma=24$), where the structure was seen by going up in small ($\Delta r \sim 0.011$) steps through the Sorét regime. Figure 3 shows this structure. First we show for comparison [Fig. 3(a)] the image that the shadowgraph picks up from the conductive state at $r=0.012$. The image is seen to be smooth, with no apparent structure. We follow this by an image [Fig. 3(b)] taken at $r=0.16$, where a large-scale structure can be discerned, especially when compared with the image taken in the conductive state. We stress that the left and center images have received exactly the same treatment in the way of image enhancement (i.e., division by a reference picture, a rough elimination of linear trends, and gray shadow rescaling according to the statistical distribution of intensities in the image). To further enhance the signal of Fig. 3(b) we use a truncation in Fourier space, using the information obtained from the spectra of these images[28] (these spectra are shown in Fig. 4). Figure 3(c) was obtained from Fig. 3(b) by eliminating all spectral power above the peak centered at $k_p/2$, half the wavelength of convection in a pure fluid (k_p is equivalent to the wavelength expected for the Rayleigh mode). The large-scale structure now becomes very prominent. We see a large structure in the center of the cell, whose exact shape is nuclear and may have been distorted slightly due to the extreme enhancement of the signal. The dark signal in the center of the cell signifies downflow. This dark path is surrounded by a ring of smaller cells, giving a spokelike structure around the center of the cell. We note that the same procedure for the signal in Fig. 3(a) gave no coherent structure whatsoever.

To estimate the spectrum of the images we plot the absolute value of the Fourier components [obtained by a fast Fourier transform (FFT) algorithm]. We have transformed to polar coordinates and integrated over the angle, as a form of portraying the 2D information (k_x, k_y); Fig. 4(a) shows the spectral power of the image of the large-scale structure. We note an enhancement at low $|\mathbf{k}|$ ($\approx k_p/8$) and one around $|\mathbf{k}|=k_p/2$. The form of the peak at $k_p/2$ is sensitive to the exact procedure of analysis, and we can only be certain of its position, not of its exact shape. Also, in the images of Fig. 3 an asymmetry between the x and y directions is apparent, and is due to a misalignment in the optical components. This has been corrected for in the spectral analysis, but does increase the uncertainties in describing the peaks. As a control we show two spectra. Figure 4(b) shows the spectrum obtained from the image of the Fig. 3(a), in the conductive state. No peaks are apparent, and the spectrum is dominated by the k ($=|\mathbf{k}|$) dependence we can expect from integrating a constant over an area segment $kd\theta$. The enhancement at low k is completely missing. Notice, though that the noise at high k is lower than that in Fig. 4(a). This is due to the effect of larger fluctuations in the bath temperature on the signal. To see this we show in Fig. 4(c) the spectrum obtained from a measurement of water in the same cell, at $r=0.10$ ($\Delta T=1.47$ K, compared with $\Delta T=1.43$ K for the mixture). The level of noise is now the same as that in Fig. 4(a). However, the peak at low k is seen to be smaller, narrower, and at lower values of k than that of Fig. 4(a), and we attribute its appearing at all mainly to faulty removal of the linear trends. There is no sign of any peaking near $k_p/2$, nor do we expect any.

C. Appearance of small-scale structure

We first follow the appearance of the small-scale structure in the small aspect ratio ($\Gamma=8.9$) square cell. This is because due to the smaller time scales involved we hope

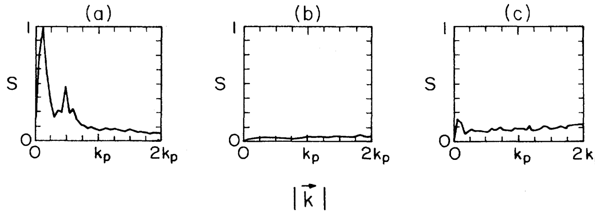

FIG. 4. Spectral power estimates obtained from the squared amplitude of the Fourier components. Square cell, $\Gamma=24$. (a) 40 wt. % of ethanol, $r=0.15$ [see image in Fig. 2(b)]. (b) 40 wt. % of ethanol, $r=0.012$ [see image in Fig. 2(a)]. (c) Pure water, $r=0.10$ ($\Delta T=1.47$ K).

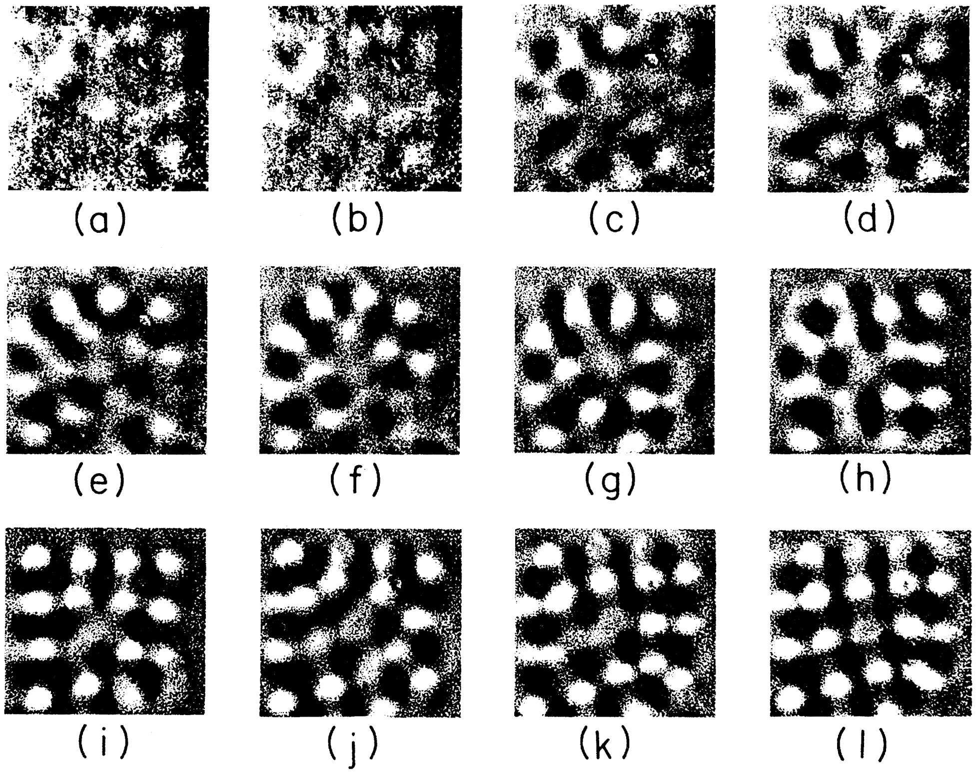

FIG. 5. Sequence of flow patterns for the $\Gamma=8.9$ square cell, $T=25\,^{\circ}\mathrm{C}$, 40 wt. % of ethanol: (a) $r=0.80$, (b) $r=0.82$, (c) $r=0.93$, (d) $r=0.96$, (e) $r=0.98$, (f) $r=1.00$, (g) $r=1.02$, (h) $r=1.04$, (i) $r=1.07$, (j) $r=1.15$, (k) $r=1.14$, (l) $r=1.12$. This sequence is shown after about one $\tau_{h,T}$ in the following time steps in $\tau_{v,T}$: (a) 0, (b) 2.5, (c) 7.5, (d) 10, (e) 12.5, (f) 15, (g) 17.5, (h) 20, (i) 22.5, (j) 27.5, (k) 32.5, (l) 39.

to see the evolution of the small-scale structure directly on top of the large-scale structure. In Fig. 5 we show 12 shadowgraph images of the patterns that appear as we consecutively change the temperature difference across the cell. The images at low values of r are too poor to be well discerned even after enhancement. Traces of the large-scale structure can be seen in Figs. 5(a) and 5(b), and immediately precede the appearance of the small-scale structure. Figures 5(c) and 5(d) show a seemingly disordered pattern of small scale ($k \sim k_p$). However, if we remember the signal in the large square cell, we can follow the symmetry of a spokelike pattern, with the signal in the center of the cell obscured, but the ring of smaller cells very clear [this is especially clear in Fig. 5(d)]. Figures 5(e)–5(j) show the slow appearance of a full small-scale pattern, and an orientational transition in the ordering of the small convection cells. We can attribute this transition to a changeover from the symmetry imposed by the large-scale structure that is dominated by the center of the cell with its surrounding spokes, to that of a square grid. This annealing procedure is a slow one, and the rate at which we change the temperature difference does not allow for complete relaxation of the pattern. This is apparent from Figs. 5(k) and 5(l) where we lowered r slightly, yet the aligning procedure continues. Note the pattern in Fig. 5(j), indicating that the annealing transition occurs through a focus defect situated at the top left corner of the cell.

Although the shadowgraph images obtained in the low Sorét regime in the process depicted in Fig. 5 yield no obvious information, their respective spectra give a much clearer picture of what is going on. This is shown in Fig. 6. We show in column II of this figure the 3D information of the 2D spectrum in a landscape format. To supplement this we use in column I a projection onto the k_x, k_y plane, and use 17 gray scales to portray spectral power on a linear scale. In this way angular distributions that may be hidden by the peaks in the landscape figures can be resolved. In column III of the same figure we show the power integrated over the angle in polar coordinates.

Already at $r=0.17$ a signal appears, similar to the one that appeared in the large square cell. An enhancement at low k along with the beginning of a peak at $k_p/2$ is seen in Fig. 6(a), and is most clear in column III. If we follow the development shown in column III we see that the peak at $k_p/2$ broadens and enhances, till at $r=0.46$ [Fig. 6(e)] it starts to overshadow the peak near $k=0$. The peak continues to broaden, and at $r=0.82$ it extends just beyond k_p. A sharp transition occurs in Figs. 6(h)–6(j), accompanied by an increase in the amplitude by orders of magnitude. This transition is connected to the appearance of the small-scale structure. At this stage the peak at $k_p/2$ disappears, and the spectrum is dominated by the peak at k_p.

The orientational transition can be followed in column I. The initial orientation is in the diagonal of the cell [Figs. 6(a)–6(e)]. Then the other directions enhance [Figs. 6(f) and 6(g)]. By the time the structure with wave number k_p comes in, the pattern is almost symmetric around the center of the cell (this is the spokelike structure). Then comes the transition to the square lattice, characterized by four prominent peaks in the spectrum.

In Fig. 7 we show for the $\Gamma=20$ circular cell the effect of bypassing the large-scale structure, going directly to the small-scale one. Figures 7(a)–7(c) show the evolution of a random initial pattern [Fig. 7(a)] obtained by stepping in short time steps to $r \approx 0.72$. This pattern evolves to the one in Fig. 7(b) at $r \approx 0.99$. The pattern in Fig. 7(c), at $r \approx 1.11$ is a stable one. The mismatch of the square grid and the circular boundaries is very pronounced, and the number of various defects is large. The

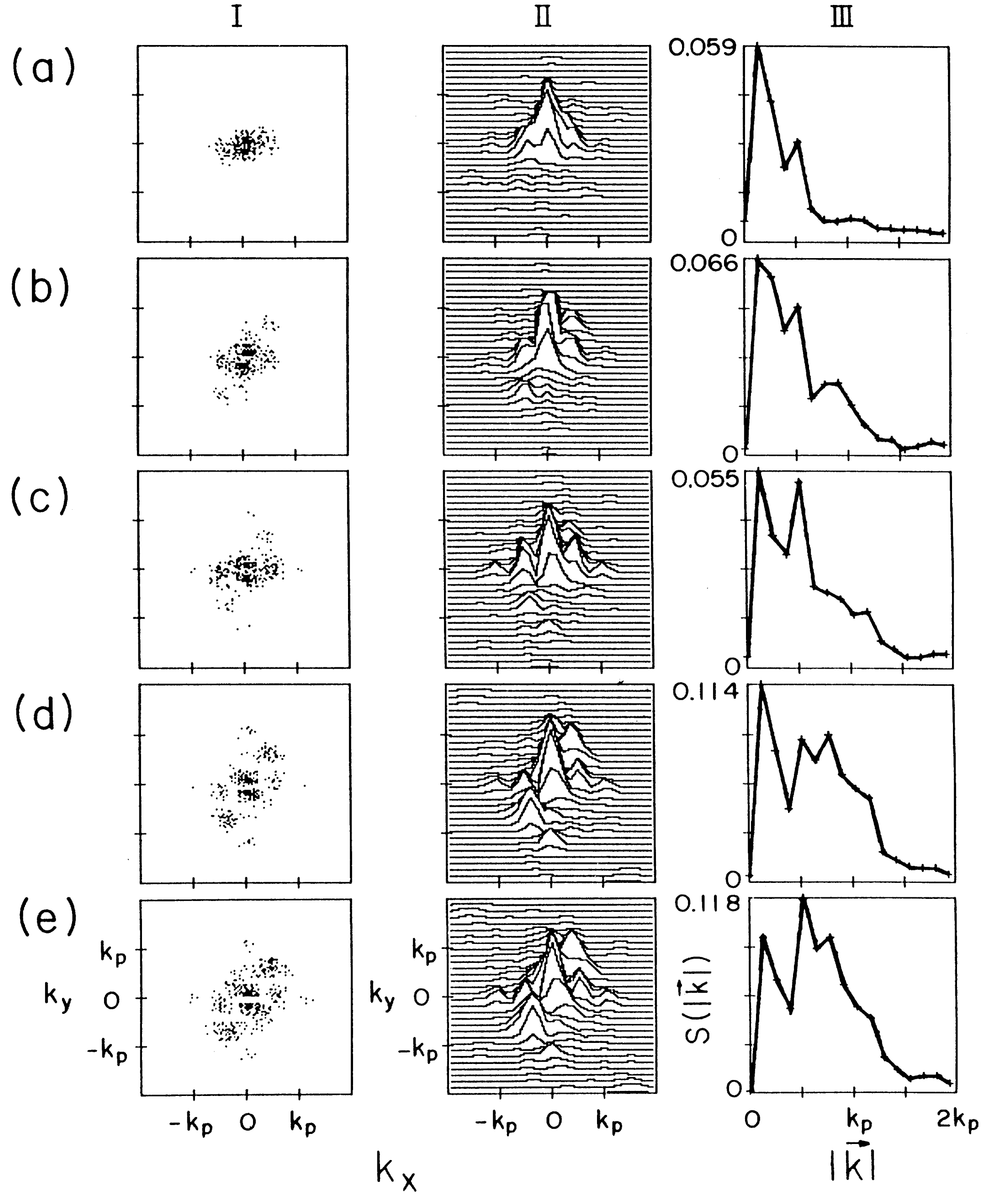

FIG. 6. Spectral power estimates obtained from the squared amplitude of the Fourier components. Square cells, $\Gamma=8.9$, $T=25\,^{\circ}\mathrm{C}$, 40 wt. % of ethanol: (a) $r=0.17$, (b) $r=0.21$, (c) $r=0.24$, (d) $r=0.40$, (e) $r=0.46$, (f) $r=0.74$, (g) $r=0.82$, (h) $r=0.96$, (i) $r=1.07$, (j) $r=1.12$. Column I is a projection onto the (k_x,k_y) plane of the spectral power. Seventeen gray scales are used in a 4×4 matrix for each (k_x,k_y) point. Column II is a landscape representation of the same data. The scales in columns I and II are identical. Each row is scaled separately. Column III is the result of an integration of the 2D data (in polar coordinates) over the angular variable. Again each row is scaled separately, and the numbers on the S axis display the power scale for each graph.

symmetry around the center of the cell that appeared in the small cell is not manifested here, since we did not give enough time for the large-scale structure to develop as an infrastructure.

A different approach is used in Figs. 7(d)–7(f). Here we induced a set of concentric cylindrical rolls by quenching the system, going to a very high input of power [Fig. 7(d) was obtained with 3.75 times the power used in Figs. 7(c), 7(e), and 7(f)]. At this temperature difference we were actually able to see the convection rolls by eye. We waited a few minutes, ensuring the pattern had the required symmetry, then reduced the power till it coincided with that of Fig. 7(c). Figure 7(e) shows the pattern after $\sim 1\tau_{h,T}$, while the relaxed pattern is that of Fig. 7(f), taken after $\sim 13\tau_{h,T}$. We note two things. First, the relaxation times for the orientational ordering are larger than the times we typically used between steps in temperature difference, and second, the patterns obtained in the two processes are very different. We have not attempted a classification of the annealing processes that lead to the final patterns, or of the defects that appear in these final states in any of the cells used.

Figure 8 shows the evolution of the small-scale pattern in the $\Gamma=24$ square cell. An initial random aggregation of squares is seen in Fig. 8(a), and more and more cells appear as r is raised. In Figs. 8(e)–8(g) we observe the an-

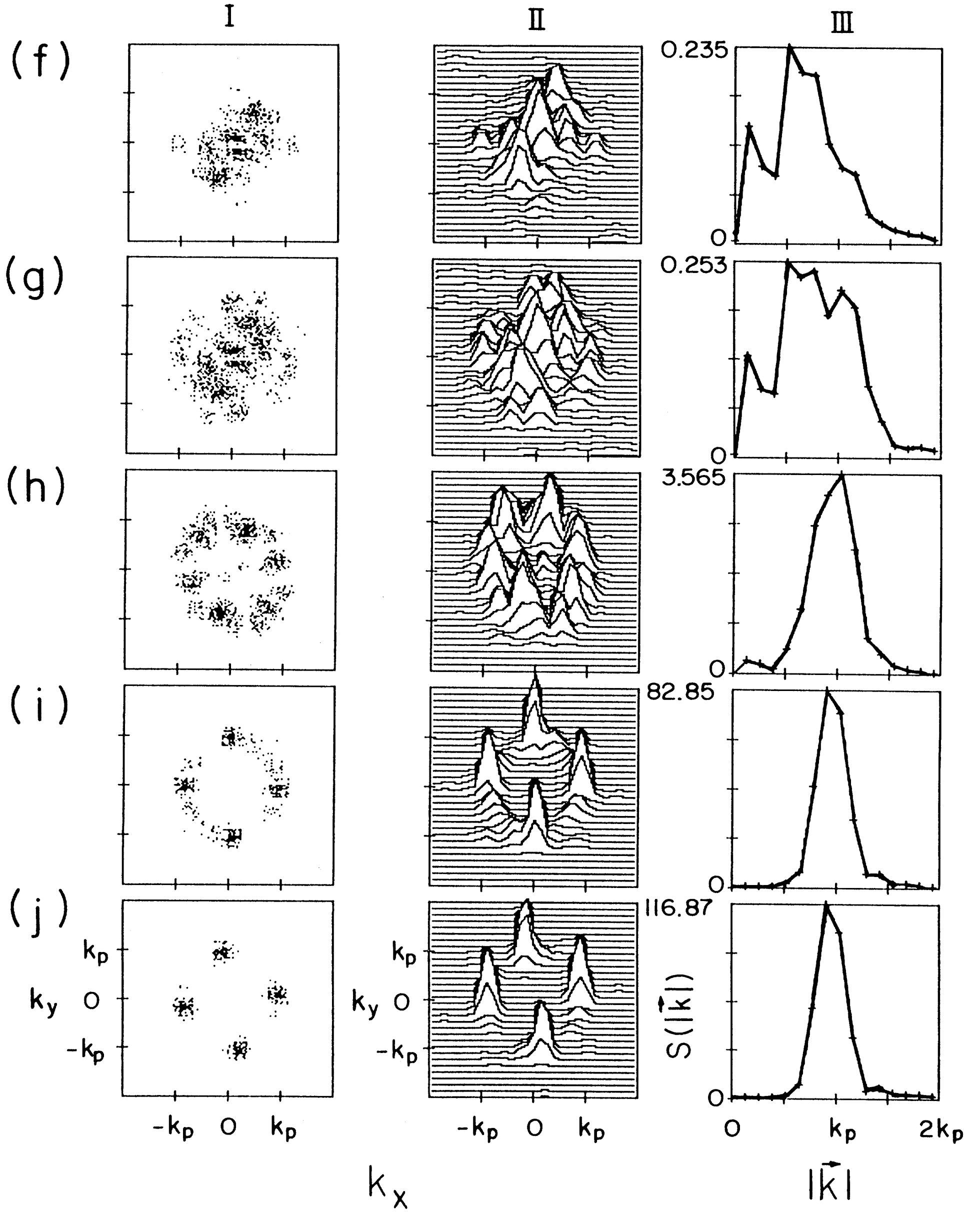

FIG. 6. (*Continued*).

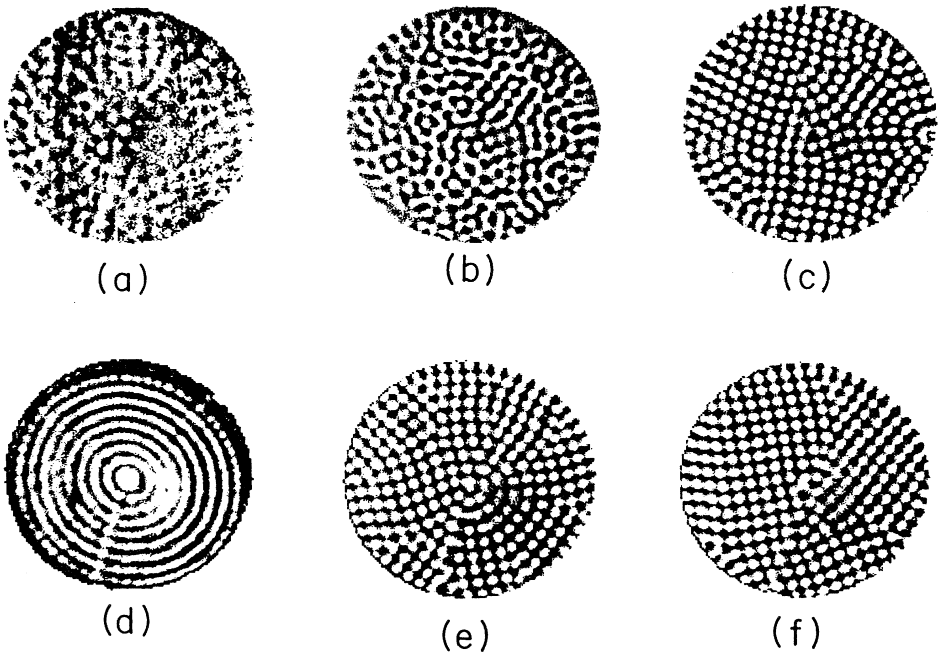

FIG. 7. Flow patterns in the $\Gamma=20$ circular cell at $T=25\,^{\circ}\mathrm{C}$, $C=40$ wt. % of ethanol. (a)–(c) are sequential in time, as are (d)–(f). (a) Heat input $q=1$ (arbitrary units), $r\approx0.72$. (b) $q=1.4$, $r\approx0.99$. (c) $q=1.6$, $r\approx1.10$. (d) $q=5$, temperature not relaxed. Time $t=0$. (e) $q=1.6$, $t\sim1\tau_{h,T}$. (f) $q=1.6$, $t\sim13\tau_{h,T}$.

nealing process, whose onset occurs when the convection cells begin to touch each other, and to feel the influence of one another. The annealling process is not completed until the pattern of Fig. 8(l). This image is taken at a regime where a new phenomenon appears, that of oscillations between the two sets of rolls that comprise the square pattern. The stable pattern is in this case a square grid rotated with respect to the borders of the square cell.

D. Oscillations between the two perpendicular sets of rolls

At the transition region to the Rayleigh regime we observed oscillations of the type seen in Ref. 22. The square structure at the point in which oscillations set in has the k_p wavelength, and can be viewed as two perpendicular sets of rolls. The oscillations are between domination of one or the other of these sets of rolls. In between domination by each set of rolls the system goes through a state of equal strength of both sets of rolls, i.e., the pattern is a square one.

Figure 9 shows the oscillatory behavior in the shadowgraph images of the circular cell. Figure 9(a) depicts the initial square pattern, for r below the onset of oscillations. The pattern is divided into many domains that do not anneal, due to the mismatch with the boundaries. The full cycle [Figs. 9(b)–9(e)] lasts about $42\tau_{v,T}$, and we show the state at $10.5\tau_{v,T}$ intervals, using video slicing (two gray scales only) to enhance the contrast. We see, for example, in the domain in the left center of the image, the cycle: horizontal rolls [Fig. 9(b)], squares [Fig. 9(c)], vertical rolls [Fig. 9(d)], squares [Fig. 9(e)], and back to vertical rolls [Fig. 9(f)]. The oscillations are dominated by the domain structure. The roll structure that gains domination begins to do so at the boundaries of the cell, forms a front that propagates into the cell, moving till it stops at the domain boundaries. Therefore the exact time dependence in each domain depends on its shape and size, and we conclude that for studying the details of the oscillations we must use a coherent structure.

To do so we followed the example of Ref. 22, using the induction of a structure by using a grid of external heating.[29] Even so, due to the large ΔT at which we worked in these thin cells, we were only able to induce approximately symmetric structures. We could then use square cells, where the natural tendency for annealing produced perfect square grids that we could use. We used intermittent external heating (to avoid overheating) by an infrared lamp through a grid of vertical strips of width d, and simultaneously raising the temperature difference continuously from conduction to the regime of small squares (i.e., $r\sim1$). We then left the structure to anneal over a period of $4.4\tau_{h,T}$. The result is shown in Fig. 10(a) for the $\Gamma=24$ square cell.

In Fig. 10(b) we show, as an aside, the same pattern after raising ΔT to about twice the temperature difference, in order to force the system into the roll pattern. We note that although one set of rolls is somewhat more vivid in Fig. 10(a), it is the perpendicular set that dominates the far Rayleigh regime in Fig. 10(b). Also, while this set dominates the cell following the end of the

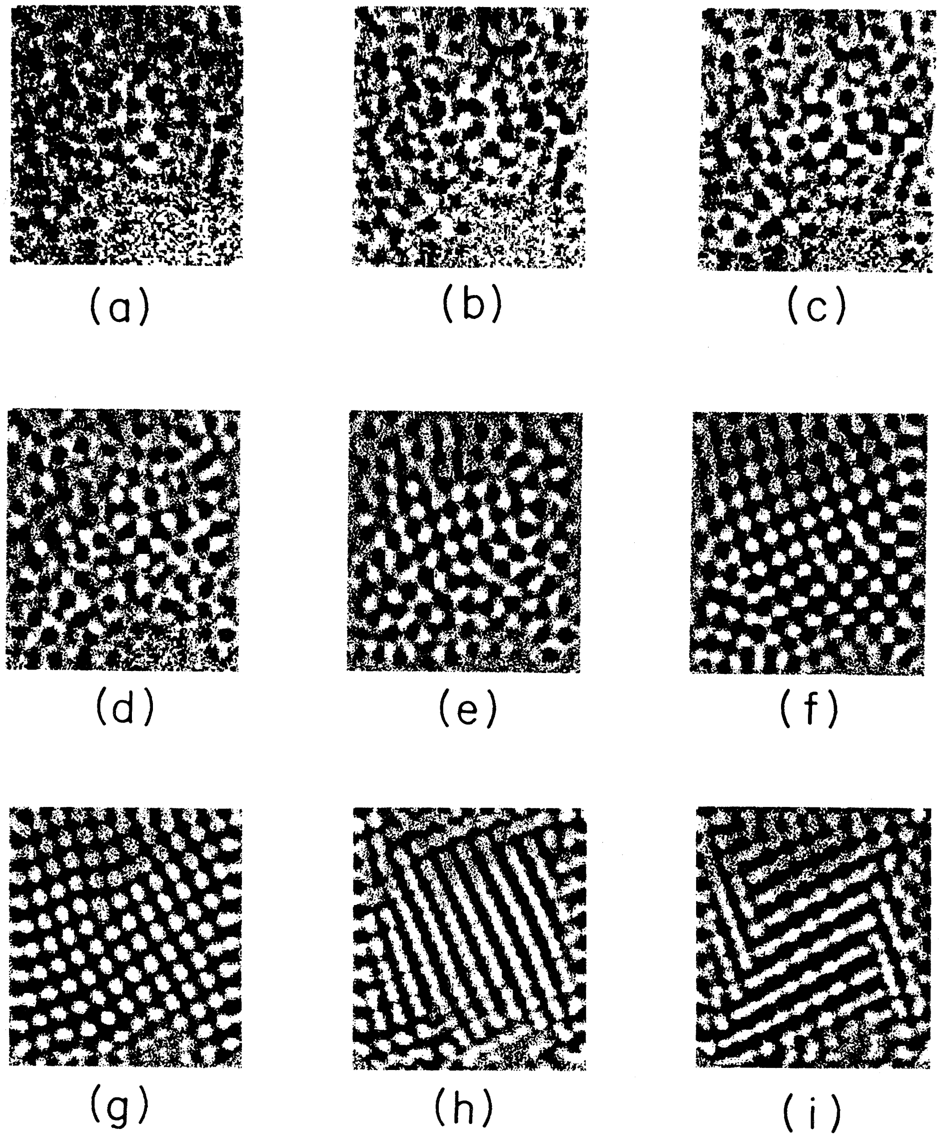

FIG. 8. Sequence of flow patterns for the $\Gamma=24$ square cell at $T=25\,^{\circ}\mathrm{C}$, 40 wt. % of ethanol: (a) $r=0.67$, (b) $r=0.74$, (c) $r=0.81$, (d) $r=0.89$, (e) $r=0.96$, (f) $r=1.02$, (g) $r=1.12$, (h) $r=1.21$, (i) $r=1.25$.

oscillations, the other set of rolls can still be discerned for quite a span of r. Referring back to Fig. 2, the arrow points at the onset of oscillations, and along the points till the end of the graph square pattern are to be found (compare this with the rectangular cell below). The pure roll formation lies in a region not included in the scale of Fig. 2.

Figures 10(c)–10(e) show half a cycle of the oscillations. We start with a set of horizontal rolls in Fig. 10(c). The vertical set of rolls starts to dominate at the two opposite horizontal boundaries, from where they propagate into the cell in the form of a spearhead front [Fig. 10(d)], till the two fronts meet at midcell [Fig. 10(e)]. As r is increased the oscillations become relaxational. They are highly nonlinear, and the transition from one set of rolls to the other is very fast, followed by a relatively long period of domination by one of the rolls. In this case the square pattern is very quickly swept through, and the system lies most of the time in the roll patterns. A complete analysis of these oscillations can be found in the work of Le Gal.[30]

The details of the oscillations are shown in Figs. 11–13. Figure 11 shows the shadowgraph signal at one chosen point in the cell. As noticed also in Ref. 16, this results in an arbitrary addition of the amplitudes of the two sets of perpendicular sets of rolls. The point we have chosen lies close to, though not exactly on, a point where the two amplitudes are symmetric (such points form a grid rotated by 45° with respect to the grid of the convective pattern). In fact, close to the onset of the oscillations the

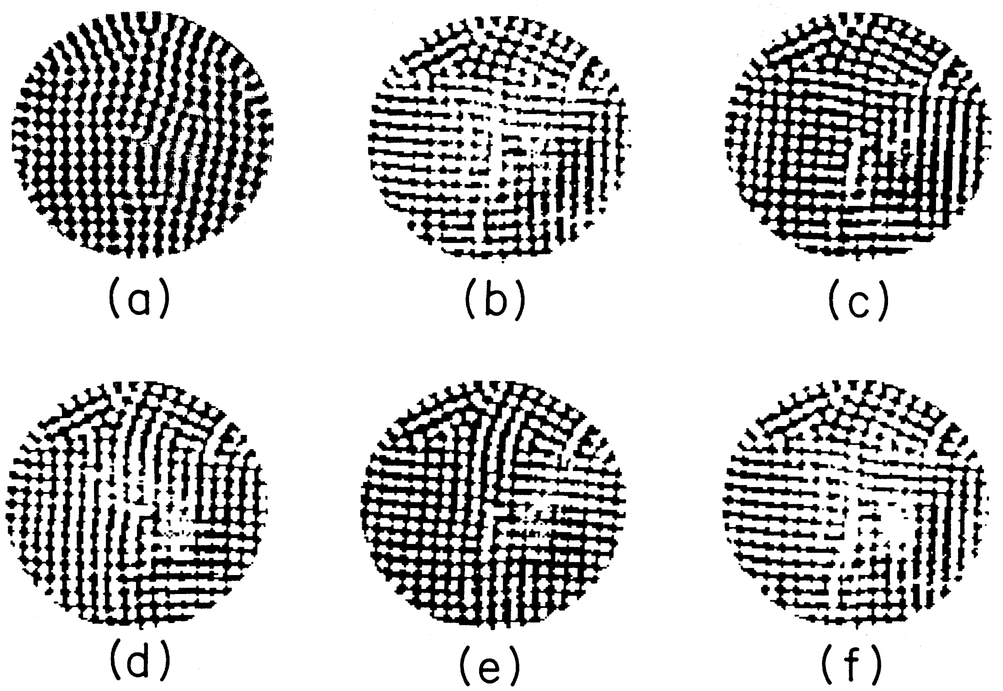

FIG. 9. Flow patterns in $\Gamma = 20$ cylindrical cell at $T = 25\,^{\circ}\mathrm{C}$. 40 wt. % of ethanol: (a) ordered square pattern at $r \simeq 1.10$; (b)–(f) pictures of oscillating square patterns at $r \simeq 1.19$. The time sequence for pictures during the cycle is $t = 0$ for (b), $t = 10.5\tau_{v,T}$ for (c), $t = 21\ \tau_{v,T}$ for (d), $t = 31.5\tau_{v,T}$ for (e), and $t = 42\tau_{v_1T}$ for (f).

stronger of the two amplitudes in the signal is the one which will later die out.

The main features of the oscillations are apparent in this figure. The amplitude of the oscillations grows continuously, while the frequency sets in at a finite value. At onset the oscillations are symmetric, almost sinusoidal, and then become more and more anharmonic as their amplitude grows. Finally, they become very asymmetric and relaxational, with very short transition times between states of domination by the opposing sets of rolls.

Figure 12 shows the corresponding r measurements for the four upper curves in Fig. 11. Oscillations appear with

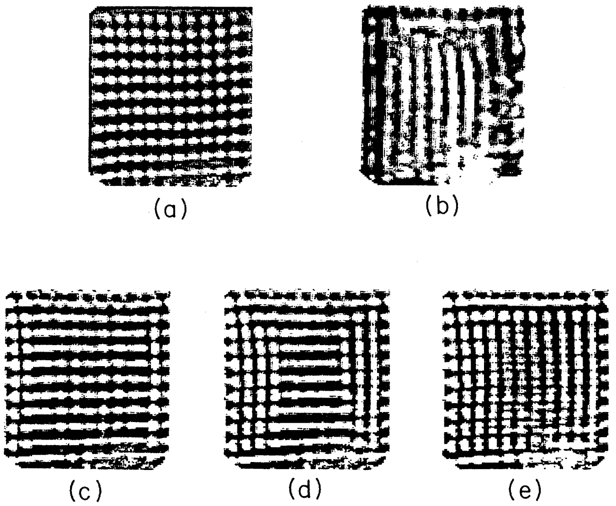

FIG. 10. Flow patterns in $\Gamma = 24$ square cell at $T = 25\,^{\circ}\mathrm{C}$, 40 wt. % of ethanol: (a) induced "perfect" square grid at $r = 1.07$; (b) roll pattern at $r \simeq 2.6$, (c), (d), (e) sequential pictures of the oscillating structure at $r = 1.19$. The time difference between pictures is $12.5\tau_{v,T}$.

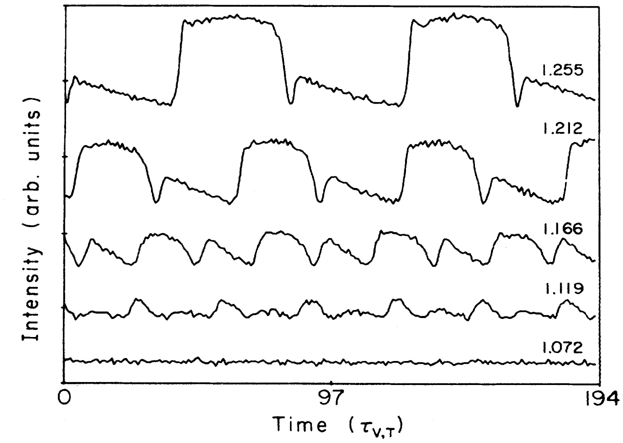

FIG. 11. The light intensity of the shadowgraph at a chosen location in the large square cell with 40 wt. % of ethanol for five different values of r. The numbers given on the figure are averaged values of r.

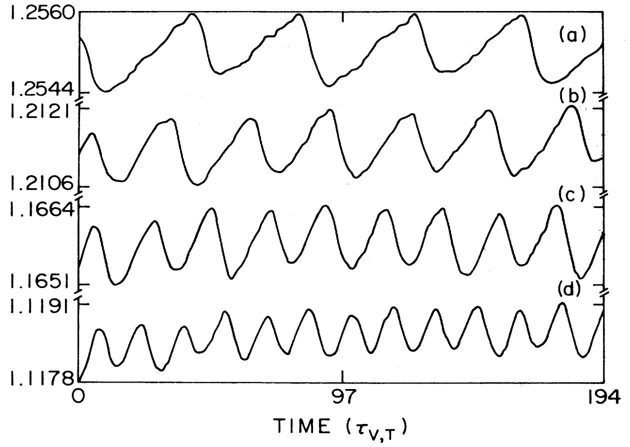

FIG. 12. The time dependence of the bottom plate temperature in the large square cell with 40 wt. % ethanol for different values of averaged r that correspond to the data in Fig. 11. (a) $r=1.255$, (b) $r=1.212$, (c) $r=1.166$, (d) $r=1.119$.

double the frequency as the corresponding one in Fig. 11, for each curve respectively. As suggested in Ref. 16 we can try to estimate the degree of experimental asymmetry of the two sets of rolls from their effect on the Nusselt number (in this case N is proportional to r^{-1}). This effect is largest at the minima of ΔT, when the rolls are at their (respective) maxima. A slight drift that is much higher than our long time measured drift exists in the data, but even so a systematic effect does appear, where the minima corresponding to the one set of rolls (the one that will die out) are consistently lower (i.e., the convection in this direction is by about 10% more effective).

In Fig. 13 we give the measured frequencies for the same cell and mixture. We cannot characterize the functional dependence of the frequency as stemming from a known model. An interesting point is that of the time scale characterizing the oscillations at their onset. This time scale lies in between the vertical and horizontal thermal diffusion times ($\sim 27\tau_{v,T}$ or $\sim 0.04\tau_{h,T}$), and can probably not be attributed to either of these time scales.

The data in Fig. 14 strengthen this view on the time scales. Shown are the oscillations that occur when we use a perfect grid in the $\Gamma=8.9$ square cell. Figure 14(a) shows the initial pattern before the onset of oscillations. Figures 14(b) and 14(c) are video sliced images of the oscillating patterns, with the time between then $12\tau_{v,T}$. We see that although the horizontal scales are different, the time scales remain in the same vicinity. We note that in Ref. 22 the time scales were much longer, comparable only to the horizontal thermal diffusion time, while in the numerical simulation of Ref. 16 the time scales were shorter by about a factor of 10. We tend to tie the oscillation frequency with properties of the fluid, not with the geometry of the cell. A further interesting feature of Figs. 14(b) and 14(c) is the fact that only a small part of the pattern oscillates, the central rolls in each of the two sets of perpendicular rolls, while the rest of the pattern is fixed, probably by the boundaries.

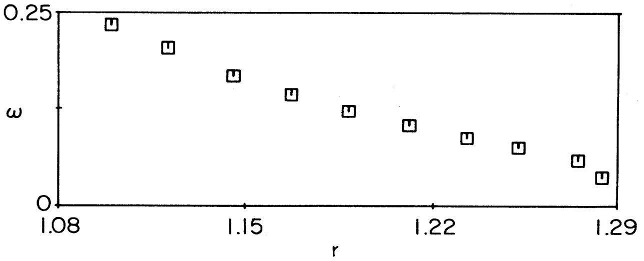

FIG. 13. The frequency (in dimensionless units) of light intensity oscillations as a function of r.

E. Effect of a restrictive geometry

The effect of asymmetry on the square pattern can be checked by giving one roll direction an advantage. This can be done in a cell with one long and one short boundary (the rolls will try to orient themselves perpendicular to the sides). Figure 15 shows three typical patterns observed in a rectangular cell with aspect ratio 1:4:12. The first pattern [Fig. 15(a)], a random square one, we observed close to ΔT_p, but still in the Sorét regime. The second pattern [Fig. 15(b)] reflects the transition to rolls, and occurred in the region of the transition to large S corresponding to the Rayleigh mode. The third pattern [Fig. 15(c)] clearly shows the usual Rayleigh-Bénard convection roll structure and was observed very close to ΔT_p, but already in the Rayleigh regime. Note that in the $\Gamma=24$ square cell a square pattern was still observed for values of $N-1$ as high as 20 times the value corresponding to this pattern.

All three types of patterns are stationary, and oscillations were not observed in these cells at all. We find that the geometry of the rectangular cell puts strict limitations on the competition between mechanisms. For this geometry the transition to the Rayleigh mode brings with it the transition in patterns. The fact that we did not see any large-scale structure can be attributed to the height of the cell, which reduced our resolution in the shadowgraph. However, the fact that no annealed structure was observed, that there was no oscillation region, and that the roll structure almost immediately became the preferred one,indicates that the selection of one set of rolls by the cell geometry has a profound effect on the nature of the pattern selection and competition.

V. DISCUSSION

This work is basically a case study of pattern selection due to the effect of horizontal boundary conditions. Although this is hidden within the interplay between the two mechanisms of convection and in the Sorét effect, we are actually watching a system that undergoes a gradual transition in the boundaries that affect it as we raise the Rayleigh number. Thus the large-scale structure that we

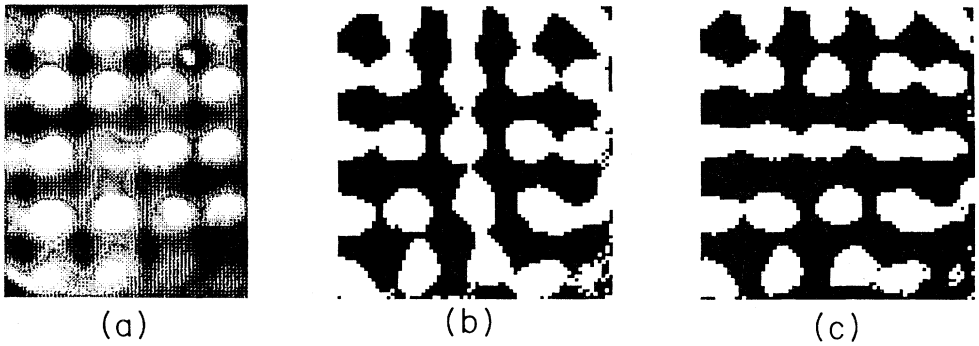

FIG. 14. Flow patterns in $\Gamma=8.9$ square cell at $T=25\,^{\circ}\mathrm{C}$, 40 wt. % of ethanol: (a) square lattice at $r\approx1.09$; (c) oscillating structure at $r\approx1.11$. The time difference between pictures is 10 min.

observed at onset is linked to a small "effective Biot number." The transition to smaller cells at larger amplitudes can be viewed as a change in this "effective B." The work of Ref. 16 on the relative amplitudes of the thermal and concentrationlike fields supports this view of the transition in scales. However, in Ref. 16 the wave number is taken to be constant, at k_p, so the direct comparison can be made.

The spectrum of the wave numbers in the large-scale structure is dominated by an enhancement at low k, and a smaller single broad (within our resolution) peak at $k=k_p/2$. It symmetry seems to be closer to that of rotations round the center rather than the expected D_4 symmetry. We cannot follow the development of the large-scale structure, as the signal is too small for a detailed enough study. We pick up the trail when the transition

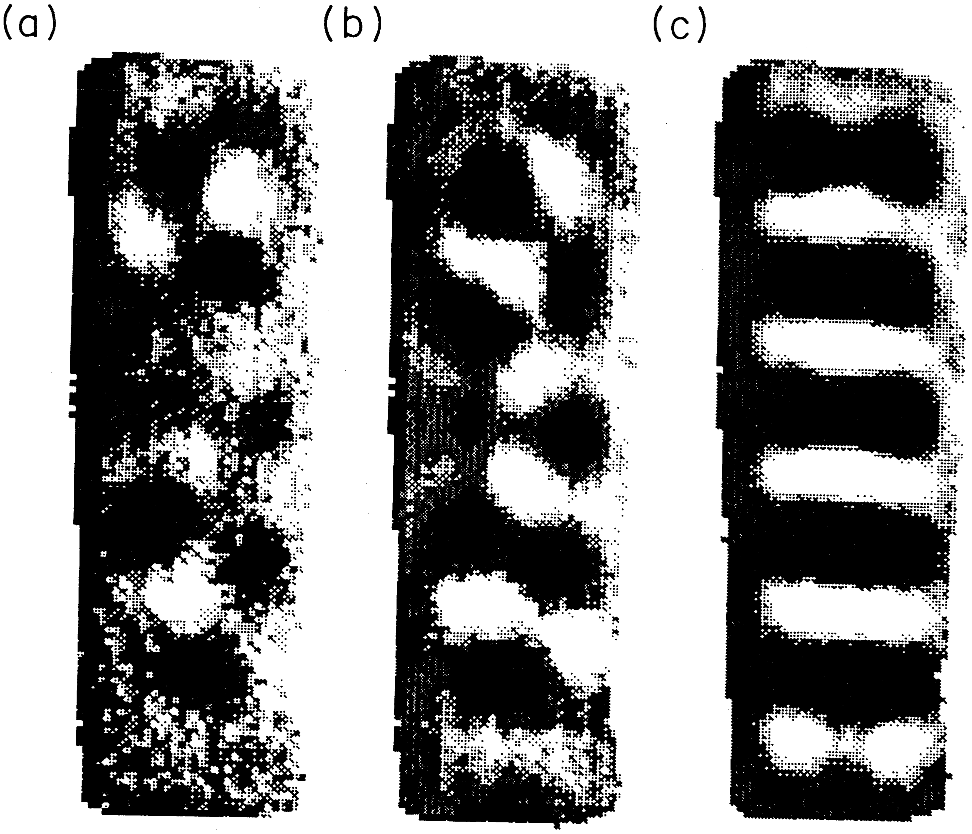

FIG. 15. Flow patterns in rectangular cell for 35 wt. % of ethanol: (a) squarelike pattern at $r=0.95$; (b) pattern in crossover region at $r=1.01$; (c) roll pattern at $r=1.07$.

to squares with length scale of order $2\pi/k_p$ comes in, accompanied by larger amplitudes. The appearance of the small-scale structure leads to an annealing process that lasts over times scales of $\tau_{h,T}$. A similar transition in length scales has been seen in the recent work on cyclohexane-methanol.

As we cross over into the Rayleigh regime, a Hopf bifurcation occurs, leading to oscillations between the two perpendicular sets of rolls that comprise the square structure. The oscillations are symmetric and sinusoidal at onset, then become more and more nonlinear. We found no intrinsic way to characterize the time scale of the oscillations. These oscillations have been reproduced in a numerical simulation, and shown to be inherent to the transition in binary mixtures from the square patterns of the Sorét regime to the roll patterns that occur in the Rayleigh regime. We speculate whether this mechanism is more general, in cases where two identical but rotated patterns coexist. The Hopf bifurcation may provide a general route by which one of these two patterns can win out and dominate the system.

We have seen that the behavior in rectangular, quasi-1D cell is markedly different, inhibiting an ordered grid and the oscillator behavior, and forcing an immediate transition to the roll structure. This stresses the importance of the side walls, as recognized in Ref. 16, but seems to indicate that the infinite unrestricted system will tend to squares, as suggested by Ref. 15.

Finally, in the Rayleigh regime we retrieve the pure fluid behavior in the Nusselt number. The pattern takes longer to adjust, and the remnants of the square pattern remain till deep in the Rayleigh regime, where the roll structure eventually dominates, as in the pure fluid.

ACKNOWLEDGMENTS

It is a pleasure to thank H. Brand, S. Ciliberto, V. Croquette, E. Domany, and J. Fineberg for helpful discussion and assistance. This work was supported by a U.S.-Israel Binational Scientific Foundation grant and the Minerva Foundation.

APPENDIX

In order to estimate what is the maximal size of the large-scale structure that can be detected by the shadowgraph visualization technique let us estimate first the gray scale resolution of the optical signal achievable by an eight-bit digitizer.

As is well known the measured light intensity distribution of the shadowgraph image at a distance l from the convective fluid layer is given by[31–33]

$$I(x,y,l)=\frac{I_0}{1-l/F} \tag{A1}$$

where I_0 is the light intensity distribution of the incident beam before passing through an inhomogeneous refractive field, and F is the focalization distance of the pattern:

$$F^{-1}=\left[\frac{\partial^2}{\partial x^2}+\frac{\partial^2}{\partial y^2}\right]\int_0^d \frac{n'(x,y,z)}{n_0} . \tag{A2}$$

Here $n'(x,y,z)$ is the perturbation of the refractive field due to convective flow. This problem is generally a nonlinear one since the optical path is defined by a nonlinear equation. However, if an image plane is located far enough from the caustic point, so that $l/R \gg 1$, the problem can be linearized and one gets

$$\frac{\Delta I}{I_0}=l\left[\frac{\partial^2}{\partial x^2}+\frac{\partial^2}{\partial y^2}\right]\int_0^d \frac{n'(x,y,z)}{n_0}dz . \tag{A3}$$

It is obvious from Eq. (A3) that the shadowgraph visualization corresponds to a local lens effect with a local focalization distance F being equal to the local curvature of the refractive field. For $l/F \lesssim 1$ the light intensity distribution is mapped by the nonlinear transformation of the initial light intensity and a numerical procedure should be used.[33] At this point in order to calculate the resolution of the shadowgraph according to Eq. (A3) one needs information about the refraction field perturbation $n'(x,y,z)$ due to the convective flow. This perturbation results from the temperature and concentration field perturbation which can be obtained from the convection equations for binary mixtures. These equations can be written in a nondimensional form as[3]

$$\Delta^2 U_z+\Delta_2[(1+\Psi)\Theta+\zeta]$$

$$=P^{-1}\left[\frac{\partial}{\partial t}\Delta U_z+\zeta(U_x,U_y,U_z)\right] ,$$

$$\Delta\Theta+RU_z=\frac{\partial\Theta}{\partial t}+(\mathbf{U}\nabla)\Theta , \tag{A4}$$

$$\Delta\zeta-\frac{\Psi}{L}\Delta\Theta=L^{-1}\left[\frac{\partial\zeta}{\partial z}+(\mathbf{U}\nabla)\zeta\right] .$$

The scaled units here are d, d^2/k, $\nu\kappa/\alpha g d^3$, $\nu\kappa/\beta g d^3$, and $\zeta=C-\Psi\Theta$, $R=\Delta T\alpha g d^3/\nu\kappa$, $\Psi=-(k_T/T)(\beta/\alpha)$, $P=\nu/k$, $L=D/\kappa$, and $\Delta_2=\partial^2/\partial x^2+\partial^2/\partial y^2$. Boundary conditions are $U_z=\partial U_z/\partial z=\Theta=\partial\zeta/\partial z=0$ at $z=\pm\frac{1}{2}$. The linearized problem of stationary convection is described by the left-hand side of Eq. (A4). In the Sorét regime $\Psi L^{-1}\gg 1$ (which corresponds to the case we consider) and one can use $\zeta=(\psi/L)\Theta$, reducing the problem exactly to the problem of convection in a pure fluid with thermally insulating boundaries with the eigenvalue $\tilde{R}\equiv R\Psi/L$ where $\tilde{R}_c=720$ and $k_c=0$ for an infinite horizontal plane layer (in an infinite geometry $k_c\approx\Gamma^{-1}$ where Γ is the aspect ratio). The corresponding nonlinear problem provides the expression for the concentration perturbation at small k as[11]

$$\zeta(x,y,z)=A\tilde{R}_c\frac{L}{\Psi}k^2\sqrt{\epsilon}f(z)\cos k_x x\,\cos k_y y \tag{A5}$$

where the coefficient A is on the order of one.[34]

In the case of $\Psi L^{-1}\gg 1$ the refractive index perturbation can be written as

$$n'(x,y,z)=\frac{\partial n}{\partial c}\frac{\nu\kappa}{\beta g d^3}\zeta(x,y,z) . \tag{A6}$$

Then the expression for the amplitude of the shadowgraph resolution looks like

$$\left[\frac{\Delta I}{I} \right]_{\rm ampl} = l \frac{\frac{1}{n}\partial n/\partial c}{\frac{1}{\rho}\partial \rho/\partial c} k^4 \tilde{R}_c \frac{L}{\Psi} \frac{\nu\kappa}{g d^4} \sqrt{\epsilon} \ . \qquad \text{(A7)}$$

Here $\epsilon = (R - R_c)/R_c$, and we have used

$$\frac{1}{d}\int_0^d f(z)dz \simeq 1 \ .$$

The ratio $(\rho/n)(\partial n/\partial c)/(\partial \rho/\partial c)]$, in principle, can be estimated from the Clausius-Mosotti relation for both gases and liquids which expresses a relation between the refractive index and the density in terms of molecular constants. However, the coefficients in this relation are available only for gases. In general, one can conclude that the ratio is proportional to polarizability, and is smaller for gases and larger for liquids but sufficiently close in values.

We can now use Eq. (A7) to estimate what size of a large-scale structure (or what the smallest wave number $k \equiv 3.117/m$) we are able to detect by the shadowgraph technique with an eight-bit digitizer. The minimum sensitivity in one gray level corresponds to $\Delta I/I = 0.004$. Using values of the geometrical and physical parameters from our experiment of 40 wt. %% ethanol-water mixture at 25 °C $\kappa = 0.93\times 10^{-3}$ cm^2/sec, $\nu = 2.5\times 10^{-3}$ cm^2/sec, $D = 0.42\times 10^{-5}$ cm^2/sec, $L = 0.0045$, $P = 27$, $\beta = 0.02$, $\Psi = 0.23$, $(1/n)(\partial n/\partial c) = 2.75\times 10^{-2}$, $d = 0.18$ cm, $l = 200$ cm, $\Gamma = 24$, and $\epsilon = 1$, we obtain that the minimal wave number we can detect is $k = 3.117/m$ where $m \simeq 8$. This is consistent with the observation of the low peak in our experiment. Since in our experiment $\epsilon \approx 7$ we observed a peak at $k_{\rm min}$ with even higher resolution than one gray level.[35]

---

[1] See, e.g., V. Steinberg, J. Fineberg, E. Moses, and I. Rehberg, Physica D **37**, 359 (1986).

[2] E. Moses and V. Steinberg, Phys. Rev. Lett. **57**, 2018 (1986).

[3] D. T. J. Hurle and F. Jakeman, J. Fluid Mech. **47**, 667 (1971); V. Steinberg, J. Appl. Math. Mech. (USSR) **35**, 335 (1971).

[4] D. Gutkowicz-Krusin, M. A. Collins, and J. Ross, Phys. Fluids **22**, 1443 (1979); **22**, 1457 (1979).

[5] B. J. A. Zielinska and H. R. Brand, Phys. Rev. A **35**, 4349 (1987).

[6] E. Knobloch and D. R. Moore, Phys. Rev. A **37**, 860 (1988).

[7] E. M. Sparrow, R. J. Goldstein, and V. K. Jonsson, J. Fluid Mech. **18**, 513 (1964).

[8] H. Brand, P. C. Hohenberg, and V. Steinberg, Phys. Rev. A **30**, 2584 (1984).

[9] G. Veronis, J. Mar. Res. **23**, 1 (1965).

[10] G. Ahlers and I. Rehberg, Phys. Rev. Lett. **56**, 1373 (1986).

[11] F. H. Busse and N. Riahi, J. Fluid Mech. **96**, 242 (1980).

[12] M. R. E. Proctor, J. Fluid Mech. **113**, 469 (1981).

[13] V. L. Gerstberg and G. I. Sivashinsky, Prog. Theor. Phys. **66**, 1219 (1981).

[14] D. R. Jenkins and M. R. E. Proctor, J. Fluid Mech. **139**, 461 (1984).

[15] M. Silber and E. Knobloch, Phys. Rev. A **38**, 1468 (1988).

[16] H. W. Müller and M. Lücke, Phys. Rev. A **38**, 2965 (1988).

[17] G. Knobloch, Phys. Rev. A **40**, 1549 (1989).

[18] G. Ahlers, P. C. Hohenberg, and M. Lücke, Phys. Rev. **32**, 3493 (1985).

[19] I. Rehberg and G. Ahlers, Phys. Rev. Lett. **55**, 500 (1985).

[20] H. Gao and R. P. Behringer, Phys. Rev. A **34**, 697 (1986).

[21] A. Gorius, B. Perrin, and S. Fauve, J. Phys. (Paris) Lett. **46**, L295 (1985).

[22] P. Le Gal, A. Pocheau, and V. Croquette, Phys. Rev. Lett. **54**, 2501 (1985).

[23] P. Le Gal, A. Pocheau, and V. Croquette (private communication).

[24] O. Lhost, Ph.D. thesis, Université d'Etat Mons, 1986; J. K. Platten, D. Villers, and O. Lhost, in *Laser Anemometry in Fluid Mechanics*, edited by R. J. Adrian *et al.* (Instituto Superior Technico, Lisbon, 1988), Vol. III, pp. 245–260; O. Lhost and J. K. Platten, Phys. Rev. A **40**, 6415 (1989).

[25] P. Bigazzi, S. Ciliberto, and V. Croquette (unpublished).

[26] S. J. Linz, M. Lücke, H. W. Müller, and J. Niederlawder, Phys. Rev. A **38**, 5727 (1988).

[27] P. Kolodner, H. Williams, and C. Moe, J. Chem. Phys. **88**, 6512 (1988).

[28] C. W. Meyer, D. Cannell, G. Ahlers, J. B. Swift, and P. C. Hohenberg, Phys. Rev. Lett. **61**, 947 (1988).

[29] M. M. Chen and J. A. Whitehead, Jr., J. Fluid Mech. **31**, 1 (1968).

[30] P. Le Gal, Ph.D. thesis, Université de Paris–Sud, Centre d'Orsay, 1986.

[31] W. Merzkirch, in *Methods of Experimental Physics: Fluid Dynamics, Part A*, edited by R. I. Emrich (Academic, New York, 1981), Vol. 18, p. 345.

[32] V. Croquette, Ph.D. thesis, Université de Paris–Sud, Centre d'Orsay, 1986.

[33] S. Rasenat, G. Hartung, B. Winkler, and I. Rehberg, Exp. Fluids **7**, 412 (1989).

[34] There are recent calculations of the nonlinear coefficient in the amplitude equation which describes nonlinear stationary convection in a binary fluid [W. Schöpf and W. Zimmerman, Europhys. Lett. **8**, 41 (1989)]. These numerical calculations were performed for an infinite horizontal layer and show that the nonlinear coefficient diverges at Ψ_d where the critical wave number k tends to zero. At this point the linear solution ceases to exist. We use data from the experiment at $\Psi > \Psi_d$ where according to theory $k_c = 0$ and the amplitude of, e.g., the concentration perturbation also tends to zero. Since we worked in a finite cell the theory turns out to be inapplicable. Unfortunately, there exists no functional dependence of this nonlinear coefficient either on the wave number k of the large-scale structure or on the valueof Ψ.

[35] Our resolution was also much better due to optics used.